Mechanical Systems and Signal Processing 216 (2024) 111462

Contents lists available at ScienceDirect

Mechanical Systems and Signal Processing

journal homepage: www.elsevier.com/locate/ymssp

Twist compensated, high accuracy and dynamic fiber optic shape sensing based on phase demodulation in optical frequency domain reflectometry

Sheng Li [a,b,c,1], Qingrui Li [a,b,c,1], Zhenyang Ding [a,b,c,*], Kun Liu [a,b,c], Huafang Wang [a,b,c], Peidong Hua [a,b,c], Haohan Guo [a,b,c], Teng Zhang [a,b,c], Ji Liu [a,b,c], Junfeng Jiang [a,b,c], Tiegen Liu [a,b,c]

[a] *School of Precision Instruments and Opto-Electronics Engineering, Tianjin University, Tianjin 300072, China*
[b] *Tianjin Optical Fiber Sensing Engineering Center, Institute of Optical Fiber Sensing of Tianjin University, Tianjin 300072, China*
[c] *Key Laboratory of Opto-electronics Information Technology (Tianjin University), Ministry of Education, Tianjin 300072, China*

ARTICLE INFO

Communicated by Yaguo Lei

Keywords:
Distributed optical fiber sensing
Optical frequency domain reflectometry
Phase demodulation
Shape sensing
Twist compensation

ABSTRACT

We present a twist compensated, high accuracy and dynamic fiber optic shape sensing based on phase demodulation in Optical Frequency Domain Reflectometry (OFDR) by using multiple single core fiber based sensor (MFS). A dynamic strain sensing is realized by tracking the optical phase in OFDR and combining with the phase de-hopping filtering algorithm, and the sensing spatial resolution reaches 45 μm. In addition, in order to eliminate the influence of external twist and fluctuation of inherent spin on the shape reconstruction results, we propose an external twist compensation method and inherent spin rate calibration method, respectively. Finally, we use a circle segment method to reconstruct a 3D shape of MFS. The experimental results show that the reconstruction accuracies by the proposed external twist compensation and inherent spin rate calibration methods increase over 18 times and 20 times than those without these two methods, respectively. At the same time, comparing with the traditional cross-correlation-based method, we find that the proposed phase demodulation method has a similar reconstruction accuracy, the maximum reconstruction error is 0.61 %, whereas the shape reconstruction speed is improved by nearly 10 times. This is of great significance for the application of FOSS, which can be used for dynamic shape sensing such as intelligent soft robots, surgical robot and etc.

1. Introduction

Fiber Optic Shape Sensing (FOSS) is an innovative optical fiber sensing technology that uses a fiber optic cable to continuously track the 3D shape and position of a dynamic object in real-time without visual contact [1]. FOSS plays an important role in the fields of civil [2], mechanical [3] and aerospace engineering [4], biomedicine and medicine [5], for applications such as the structural health monitoring of civil structures and infrastructures, reconstruction of the displacement of wings in the aircraft, tracking robots and medical instruments inside the human body. It is especially important to track the shape position of dynamic objects without visual

* Corresponding author at: School of Precision Instruments and Opto-Electronics Engineering, Tianjin University, Tianjin 300072, China.
E-mail address: zyding@tju.edu.cn (Z. Ding).

[1] These authors contributed equally to this work.

https://doi.org/10.1016/j.ymssp.2024.111462
Received 14 September 2023; Received in revised form 17 March 2024; Accepted 22 April 2024
Available online 27 April 2024
0888-3270/

contact.

A considerable research effort has been dedicated to FOSS and made a lot of achievements in the last twenty years, most of them use fiber Bragg grating (FBG) [6–13]. However, FBG cannot realize truly distributed sensing and its poor sensing spatial resolution limits its further application in shape sensing. In contrast, distributed strain sensing technology based on Optical Frequency Domain Reflection (OFDR) has become one of the most potential realization methods of shape sensing with its advantages of high sensing spatial resolution and high sensitivity [14]. However, the reported OFDR-based shape sensing methods are all based on the traditional cross-correlation principle [15–17], which results in the deterioration of sensing spatial resolution and large calculation burden due to sliding window and cross-correlation processing. Therefore, a demodulation method of OFDR based on optical phase tracking is proposed and applied to high-speed dynamic strain measurement. Kreger et al. demonstrated an optical phase-based vibration detection and mapping technique using data from a commercial OFDR-based fiber sensing system [18]. Based on this, Wang et al. present a distributed high sensitivity static strain sensing method based on differential relative phase in OFDR [19]. Zhao et al. proposed a robust unwinding phase method based on density distribution to obtain low-noise unwinding phase [20]. However, literatures on dynamic shape sensing by tracking light phase changes is limited. Recently, Fu et al. demonstrated an optical fiber φ-OFDR shape sensor by using femtosecond-laser-induced permanent scatter array (PS array) multicore fiber (MCF) [21]. However, this paper ignored the effect of twist on shape sensing, and the spatial resolution dose not reach the theoretical sensing spatial resolution in OFDR due to the windowing smoothing process in phase demodulation.

Usually, the sensor in FOSS can be divided into two types: one is optical multicore fiber (MCF) [22–24] and the other is multiple single core fiber based sensor (MFS) [6,7,25]. MCF is a special fiber with multiple cores embedded in a common cladding, its advantages are high flexibility and strong embedding ability, but the small core spacing results in a low response sensitivity to bending and twisting. MFS is formed by several single-core optical fibers molded with epoxy resin [6] or fixed to a bracket [7,25]. This configuration ensures a larger core spacing and improves the measurement accuracy of curvature and twist. In addition, MFS does not require additional fan-in/fan-out devices to realize the query of each fiber. The disadvantage of MSF is that the diameter of MSF is slightly larger than MCF. Due to the high flexibility, FOSSs are oftentimes subject to twisting that generates significant errors in shape sensing. Xu et al. presented a curvature, torsion, and force sensing based on concentric tube structures with helically wrapped FBG sensors [26]. The characteristic of this sensing structure with a large diameter allows it sensitive to torsion and bending. Moreover, due to the high stiffness of the sensor, the influence of axial strain caused by temperature or tension on shape reconstruction is not considered in the model. Therefore, this model between curvature, torsion, and force is not suitable for ultra-fine flexible MFS with a small diameter. Askins et al. proposed a method to estimate fiber twist using the twisted multicore fiber grating arrays [27]. The manufacturing process of twisted MCF is constantly being improved [15,28]. Floris et al. first assessed the performance of a twisted MCF-based shape sensor in sensing twisting and proposed a theoretical method based on Saint-Venant's Torsion Theory [29]. Yin et al. developed a twist model based on spun MCF and applied it to a distributed directional torsion sensor [17]. However, most of the current reports on twist are for MCF, and this model is not suitable for MFS because the central core fiber will also produce strain during twisting process. In fact, the twist calculation method is different for MCF and MFS [30,31]. The cost of MFS with inherent spin and continuous grating is relatively lower than MCF. MFS has also been applied in commercial product of FOSS [32]. Therefore, it is necessary to establish a new twist compensation model based on MFS. In addition, the instability of the inherent spin rate of spun fiber during the manufacturing will also have a great impact on the shape reconstruction results. Especially for MFS, the inherent spin rate cannot be guaranteed during the molding process. Most of the recent approaches for shape sensing neglect this phenomenon.

In this paper, a twist compensated, high precision and dynamic fiber shape sensing technology based on OFDR phase demodulation is implemented. Firstly, we propose a phase de-hopping filtering algorithm to realize the differential phase strain demodulation with high sensitivity and high spatial resolution, and the spatial resolution of sensing reaches 45 μm. Secondly, we set up a twist compensation model for MFS based on the strain relationship of each fiber. In addition, for the influence of the fluctuation of the inherent spin rate on the shape reconstruction results, we propose a calibration method of the inherent spin rate in MFS, which further improves the shape reconstruction accuracy. The experiment results show that the reconstruction accuracies by the proposed external twist compensation and inherent spin rate calibration methods increase over 18 times and 20 times than those without these two methods, respectively. Finally, we compare shape sensing results based on the phase demodulation and traditional cross-correlation. The experimental results show that the proposed shape sensing method based on phase demodulation has a similar reconstruction accuracy compared with the traditional cross-correlation based method, whereas the shape reconstruction speed is improved by nearly 10 times.

2. Principle

A twist compensated, high accuracy and dynamic fiber optic shape sensing technology based on phase demodulation in OFDR includes three parts: Differential phase strain demodulation method with phase de-hopping filter, external twist compensation method for MFS and calibration method of the inherent spin rate. Firstly, the basic process of the shape sensing technology is briefly introduced.

2.1. Process and principle of shape sensing

The basic principle of shape sensing is that different core fibers will produce different strain responses when the shape of the shape sensing fiber changes, and shape sensing can be realized by demodulating the strain in each core fiber and combining shape reconstruction algorithm. The flow chart of the shape sensing algorithm proposed in this paper is shown in Fig. 1. Three sets of experiments are required to perform shape sensing. The shape sensing fiber is made to be in straight line state, plane bending state and any three-dimensional shape, which are used as reference group, calibration group and measurement group, respectively.

Then we can calculate the strain in each core fiber using the differential phase strain demodulation algorithm, the specific algorithm principle is detailed in Section 2.2. The strain of the calibration group is used to get the inherent spin rate information of the shape sensing fiber to realize inherent spin compensation. The specific principle is shown in Section 2.4. According to the strain of the measurement group, the inherent curvature, bending angle and external twist of the shape sensing fiber can be calculated respectively. The calculation formula of the curvature κ and bending angle θ_b are [22]:

$$\kappa = \frac{2\sqrt{\left(\sum_{i=1}^{3}\varepsilon_i\cos\alpha_i\right)^2 + \left(\sum_{i=1}^{3}\varepsilon_i\sin\alpha_i\right)^2}}{3r} \tag{1}$$

$$\theta_b = \arctan\left(\frac{\sum_{i=1}^{3}\frac{\varepsilon_i}{r}\sin\alpha_i}{\sum_{i=1}^{3}\frac{\varepsilon_i}{r}\cos\alpha_i}\right) \tag{2}$$

where ε_i represents the strain in these three outer core fibers in the shape sensing fiber, respectively, α_i is the angle between each core fiber and the x-axis of the reconstructed coordinate, and r is the core spacing of the shape sensing fiber, as shown in Fig. 2. The calculation method of external twist subjected to the shape sensing fiber will be explained in detail in Section 2.3. Then we can acquire the θ_b that compensates for the inherent spin and external twist in turn, which reflects the change of direction angle caused by the shape.

The type of the shape sensing fiber we used in this paper is MFS as shown in Fig. 2. The MFS consists of four optical fibers that are tightly wound in a spiral as inherent spin, including three peripheral fibers at 120° to each other and a central fiber. These four fibers are tightly bonded together by epoxy adhesive with a core spacing of 150 μm. Continuous gratings are etched into these fibers to enhance Rayleigh backscattering. The difference between this MFS and MCF is that MFS do not have a common cladding and four fibers in MFS are independent, so MFS don't need a fan-in/out to separate these four fiber cores.

When κ and the compensated θ_b along MFS are acquired, we can use the shape reconstruction algorithm to reconstruct the three-dimensional shape. In this paper, we use the circle segment method for shape reconstruction [12]. Compared with the conventional shape reconstruction method based on Frenet-Serret frame, this shape reconstruction method we used has a smaller computational burden due to no need for numerical solution of differential equations. At the same time, this method can reconstruct 3D curves with zero curvature and singularities namely bending direction changing, which cannot be reconstructed by Frenet-Serret frame based method [12]. The basic principle of the algorithm is that the curve is composed of many circle segments with fixed radius, and the radius and direction of the circle are calculated according to κ and θ_b of MFS at that point. By repeating this process for each given set (κ,θ_b), we can reconstruct the entire shape of MFS [10]. In the circle segment method, the length of the circle segment depends on the sensing spatial resolution of the system, so a system with a better spatial resolution can acquire higher shape reconstruction accuracy.

2.2. Principle of differential phase strain demodulation algorithm in OFDR

We briefly introduce differential phase strain demodulation algorithm in OFDR [19]. A conventional OFDR system is shown in

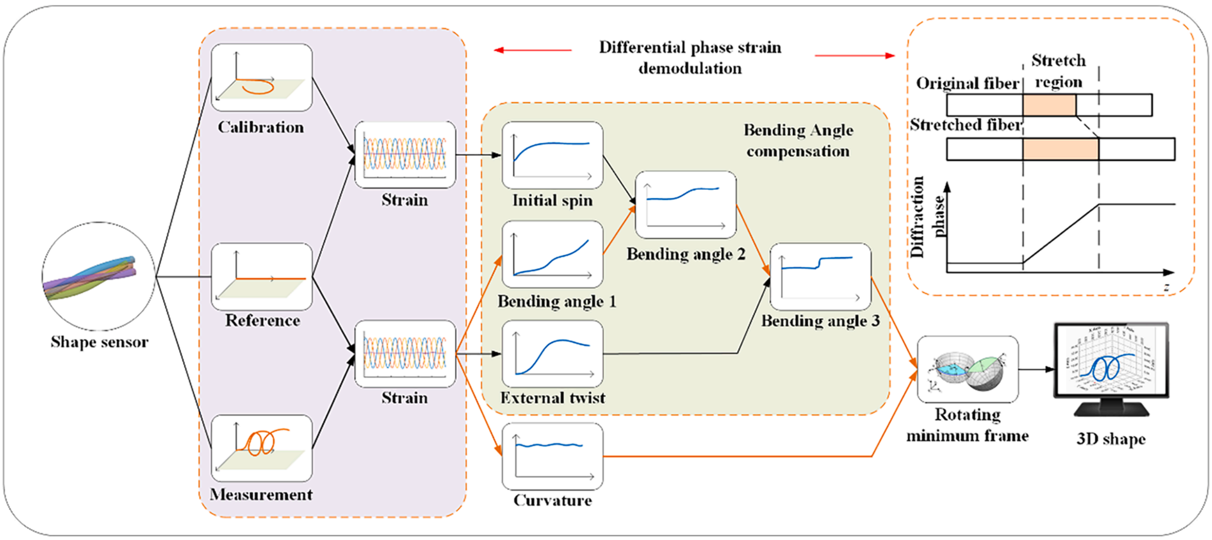

Fig. 1. Flow chart of 3D shape reconstruction algorithm.

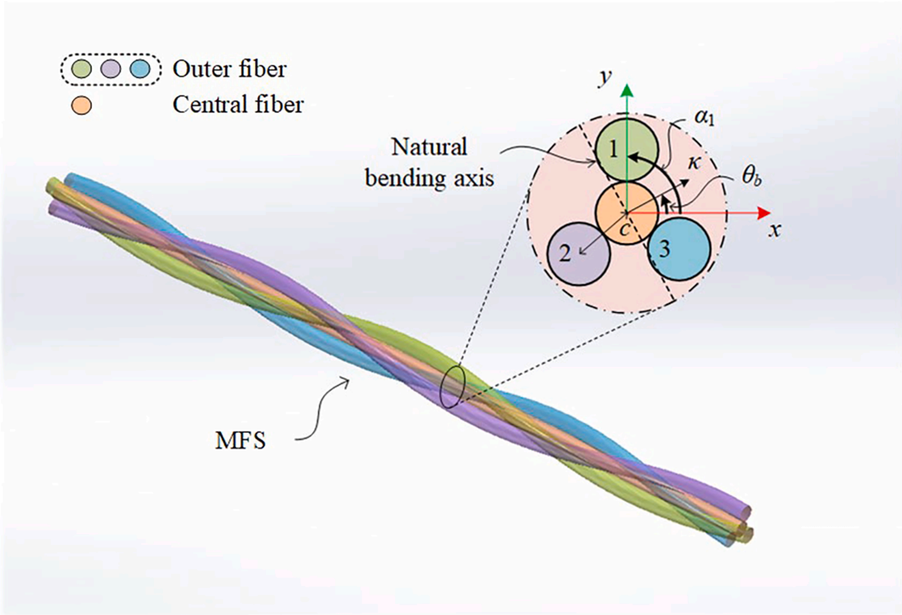

Fig. 2. Structure diagram of multiple single core fiber based sensor (MFS).

Fig. 3, which is consists of a tunable laser source (TLS) and an interferometer. By launching the light of TLS into the fiber under test (FUT), Rayleigh backscattering in FUT will interfere with the light from the local oscillator (LO), which can be detected by a photodetector (PD). When the tuning speed of TLS is γ, the beat signal of position z along FUT can be described as [19]:

$$I(t) = 2\sqrt{R(\tau_z)}E_0^2\cos\left[2\pi\left(\nu_0\tau_z + \gamma\tau_z t - \frac{1}{2}\gamma\tau_z^2\right) + \varphi_n(t,\tau_z)\right], \tag{3}$$

where E_0 is the input optical field of TLS. τ_z is the time delay at any position z. $R(\tau_z)$ is reflectivity of FUT at position z, γ is the tuning rate of TLS, ν_0 is the initial frequency, and $\varphi_n(t,\tau_z)$ is the phase noise in reference group. Since $\nu_0\tau_z \gg 1/2\gamma\tau_z^2$, the higher order term can be neglected. By FFT of Eq. (3), the corresponding phase term at corresponding position z, which can be expressed as:

$$\phi = 2\pi\nu_0\tau_z + \varphi_n(t,\tau_z). \tag{4}$$

When the fiber is stretched or compressed and assuming that the phase noise of the two sets of data before and after the strain is applied are strictly equal. The relative phase represents the length change induced by the applied strain in the fiber. The relationship between the length change and relative phase is [33]:

$$\Delta\phi_z = \frac{4\pi}{\lambda_0}\left[(1-P_e)n_{eff}\Delta L_z\right], \tag{5}$$

where P_e is the elasto-optic coefficient, λ_0 is the optical wavelength, n_{eff} is the effective refractive index, and ΔL_z is the corresponding length change. By derivative of Eq. (5), we can acquire the relation between distributed strain along FUT and the differential phase $d\phi$ is:

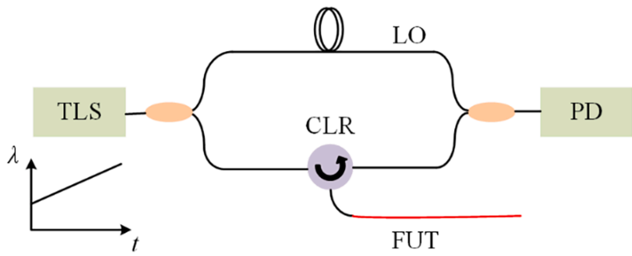

Fig. 3. Schematic diagram of OFDR system.

$$\varepsilon_z = \frac{\lambda_0}{4\pi n_{eff}(1-P_e)} diff(\Delta\phi_z) = K \cdot d\phi. \tag{6}$$

It can be seen from Eq. (6) that the strain is proportional to $d\phi$ and its proportional coefficient is K. However, due to the existence of phase noise, phase hopping occurs during phase unwrap, which eventually leads to a strain demodulation error. These phase noises may be caused by TLS's linewidth or residual nonlinearity during TLS tuning. Therefore, it is necessary to perform a de-hopping filtering to process phase data. In this paper, we propose a phase de-hopping filtering method based on probability distribution. The algorithm flow is shown in Fig. 4. By segmenting $d\phi$ and calculating the distance between each data and the median. When the distance is greater than the product of the Median Absolute Deviation (MAD) and the threshold value 1.4826, we consider this data point to be an outlier, and use the surrounding normal value for interpolation to remove these outliers. The threshold is calculated by the normal distribution function. We assume that the data follows a normal distribution $X \sim N(\mu, \sigma^2)$, and the outliers fall in the 50 % region on either side, i.e.

$$P(|X-\mu| \le MAD) = P(|\frac{X-\mu}{\sigma}| \le \frac{MAD}{\sigma}) = P(|Z| \le \frac{MAD}{\sigma}) = \frac{1}{2} \tag{7}$$

Where $P(|Z| \le \frac{MAD}{\sigma}) = \Phi(\frac{MAD}{\sigma}) - \Phi(-\frac{MAD}{\sigma}) = \frac{1}{2}$, and $P(\frac{MAD}{\sigma}) = 1 - P(-\frac{MAD}{\sigma})$. We convert MAD to a consistent estimator of σ. The threshold can be calculated as 1.4826, which is approximately equal to $1/\Phi^{-1}(3/4) = 1/0.67449$ [34]. The specific steps of the proposed differential phase strain demodulation algorithm are as follows:

1) Two groups of experiments are carried out in turn, one group of MFS is in a straight-line state, and no strain is applied as a reference. In the other group, MFS is in bent state and strain caused by bend is applied on the MFS as the measurement group. The two sets of beat signals are transformed into the spatial domain by FFT and their phase spectra are extracted as ϕ_1 and ϕ_2.
2) Subtract ϕ_1 and ϕ_2 to obtain the relative phase $\Delta\phi$ and take the derivative to calculate the differential phase $d\phi$.
3) Segment $d\phi$ along the MFS and any segment of the data is denoted as A_n, every data point in A_n is referred to a_i separately. And calculate the distance between a_i and the median of A_n separately:$\delta_i = |a_i - median(A_n)|$.
4) MAD of A_n is obtained by calculating the median of δ_i:

$$MAD = median(|a_i - median(A_n)|). \tag{8}$$

If δ_i is greater than 1.4826 × MAD, a_i is considered as an outlier and need to be removed.

5) Use the adjacent normal values to interpolate outliers to remove abnormal data points.
6) Zero-phase low pass filtering is performed to eliminate high-frequency noise in $d\phi$. According to the proportional relationship between $d\phi$ and strain applied, the distributed strain along each core fiber in MFS is calculated.

Differential phase strain demodulation algorithm in OFDR above will not reduce the sensing spatial resolution of strain sensing because no windowing or smoothing operation is applied, which can reach the theoretical sensing spatial resolution of one data point in OFDR. In addition, the calculation burden of phased based strain demodulation is greatly lower than the conventional cross-correlation algorithm. We will discuss these in detail in Chapter 3.

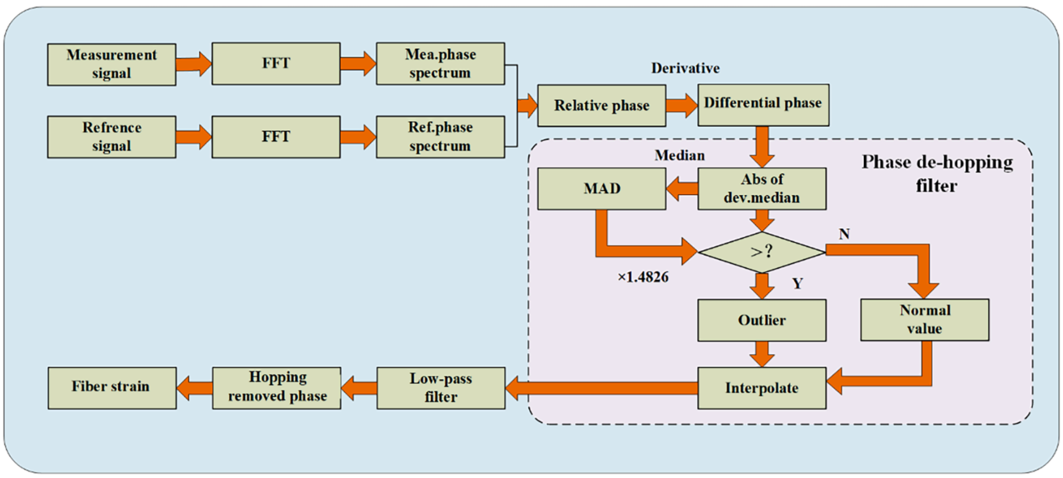

Fig. 4. Flow chart of differential phase strain demodulation algorithm with the phase-hopping filtering in OFDR.

2.3. Calibration principle of external twist of MFS

The twist force applied to MFS will cause the rotation of the outer core fiber, resulting in an error in the calculated θ_b. In order to properly map the strain of the each fiber core of MFS to the corrected bending direction, the external twist applied to MFS must be measure. Some scholars have assessed the performance of a spun MCF-based shape sensor in sensing twisting [17,29]. In MCF, strain produced only in outer cores and central core does not when MCF is twisted. Therefore, we can calculate the external twist easily from the difference between the outer core and central core. However, for MFS, both the central and outer core fiber produce stress when MFS is twisted, because they are bonded to each other tightly by epoxy adhesive. Therefore, the external twist calculation methods of MCF and MFS are different.

In order to verify the above conclusion, we experimentally measure the strain in each fiber when MFS is external twisted. The external twisting experimental setup is shown in Fig. 5. A part of 0.2 m long MFS is fixed between two optical fiber rotators. During the experiment, Rotator A is kept stationary and MFS is rotated clockwise once by Rotator B. The strain distribution signals before and after external twisting in each fiber are collected.

Fig. 6 shows the strain distribution in each core fiber when the MFS is subjected to twist only. From Fig. 6 we know that the central and outer core fiber generate reverse strain simultaneously, and the strain of the central fiber is about three times that of the outer fiber. This indicates that there is an interaction force between the central and the outer fiber when MFS is applied by an external twist. In this way, the axial tension/compression strain (common mode strain ε_a) applied to the MFS can be calculated from the mean of the strain of these four fibers:

$$\varepsilon_a = \frac{\varepsilon_1 + \varepsilon_2 + \varepsilon_3 + \varepsilon_c}{4}, \tag{9}$$

where ε_1,ε_2 and ε_3 represent the strain in three outer core fibers, respectively. ε_c is the strain applied on the central core fiber.

To acquire the relationship between external twist and the strain distribution on each fiber of MFS. A segment of full inherent spin pitch length of MFS is modeled as a cylinder show in Fig. 7. The length h of the cylinder corresponds to the inherent spin pitch of MFS, while the distance from the center core fiber to an outer core fiber represents the radius r of the cylinder. The surface of a cylinder can be represented as a rectangle if one slices the cylinder longitudinally and then flattens the surface. The length of the rectangle is h, the width is the circumference of the cylinder $2\pi r$, and the diagonal of the rectangle l_0 represents the initial length of the outer core fiber. When an external twist is loaded on MFS and assumed that the external twist direction is opposite to the initial spiral direction of MFS. The outer core fiber will have negative strain due to compression. At the same time, the central fiber will have a positive strain and be stretched due to the close contact between the outer and central core fibers. The stretch length of the center core fiber is $\varepsilon_c h$, then the strain generated by external twist in the outer fiber ε_{twist} is:

$$\begin{aligned} \varepsilon_{twist} &= \frac{l - l_0}{l_0} \approx \frac{l^2 - l_0^2}{2l_0^2} \\ &= \frac{(h + \varepsilon_c h)^2 + (2\pi r - \varepsilon_t h)^2 - (2\pi r)^2 - h^2}{2(4\pi^2 r^2 + h^2)}, \end{aligned} \tag{10}$$

where l represents the length of the outer core fiber subjected to external twist, $\varepsilon_t = \gamma_t r$ indicates the tangential strain on MFS, γ_t is the external twist rate to MFS. We assume γ_0 is inherent spin rate of MFS and submit $h = \frac{2\pi}{\gamma_0}$ into Eq. (10) and simplify Eq. (10) to get:

$$\varepsilon_{twist} = \frac{\varepsilon_c^2 + 2\varepsilon_c - 2\gamma_0\gamma_t r^2 + \gamma_t^2 r^2}{2(1 + \gamma_0^2 r^2)}. \tag{11}$$

Since γ_t is usually much smaller than γ_0. The term $\gamma_t^2 r^2$ is minuteness to be neglected compare to $2\gamma_0\gamma r^2$. Since ε_c and r are both small, $\gamma_0^2 r^2 \ll 1$ and $\varepsilon_c^2 \ll 2\varepsilon_c$. Then Eq. (11) can be approximated linearly as:

$$\gamma_t = -\frac{\varepsilon_{twist} - \varepsilon_c}{\gamma_0 r^2}. \tag{12}$$

From Eq. (12), a large r and γ_0 will lead to a high measurement accuracy of γ_t. The outer fiber is subjected to external twist, bending

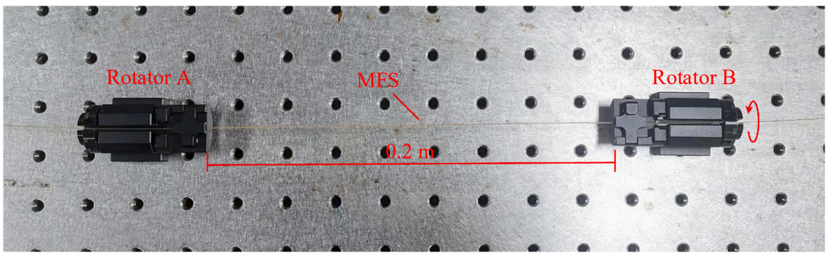

Fig. 5. Experimental setup of external twisting loaded on the MFS.

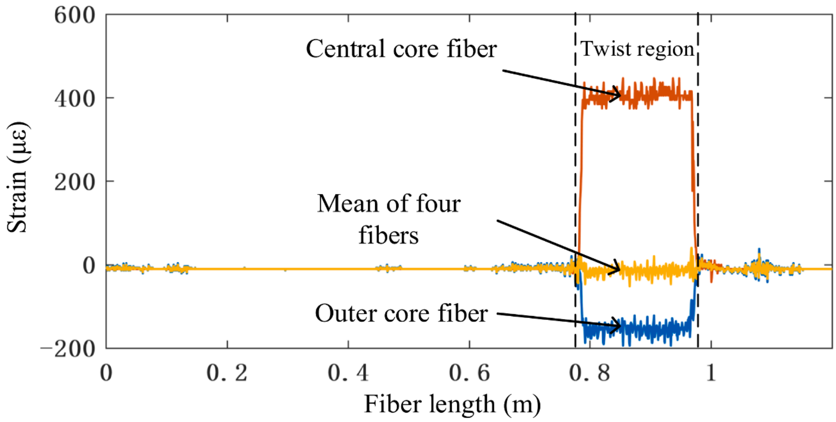

Fig. 6. Strain distribution of each fiber when MFS is subjected to external twist.

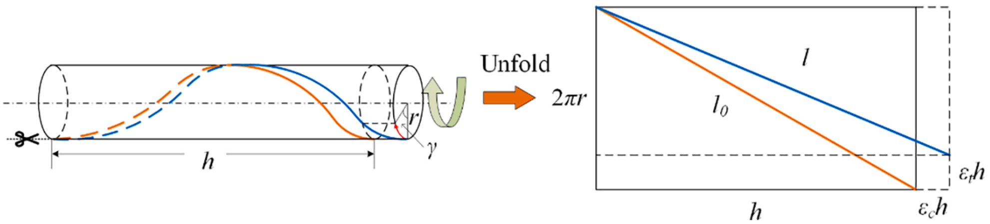

Fig. 7. Outer fiber that experiences external twist can be modeled as a flattened cylinder and unfolded into a rectangle.

and tensile strain at the same time and the sum of the bending strain of the three outer fibers is zero. Therefore, the strain caused by external twist on MFS can be calculated as:

$$\varepsilon_{twist} = \frac{\varepsilon_1 + \varepsilon_2 + \varepsilon_3}{3} - \varepsilon_a. \tag{13}$$

Combined with Eq. (9), (12) and (13), γ_t along MFS can be calculated. Then the effect of twist on the shape reconstruction can be compensated by applying the superposition principle and correcting the bending direction angle in each instrumented section according to Eq. (14):

$$\theta_b' = \theta_b - \int_0^s \gamma_t ds. \tag{14}$$

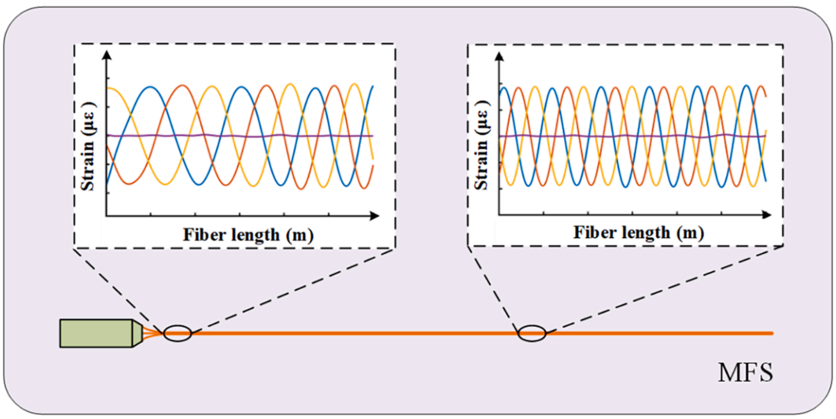

Fig. 8. Strain distribution curve of each fiber at different positions of MFS. The variation of the period of the strain distribution curve indicates that the inherent spin rate fluctuates along the MFS.

2.4. Calibration principle of inherent spin rate of MFS

To translate strain signals from the outer core fibers in to bend direction, the rotational position of an outer core fiber must be determined with a high degree of accuracy. In addition to the external twist will affect the rotation direction of the outer fiber, γ_0 of MFS is also an important parameter for calculating the bending direction of MFS. Assuming that γ_0 of MFS is constant, the α_i of the outer fibers varies linearly along the distance of the MFS. However, in practice, the fabrication of MFS introduces some variation in γ_0. Fig. 8 shows the strain response in each fiber at two different positions when MFS is bent. We intuitively find that these periods of strain distribution curve are different along MFS due to changes in γ_0 along MFS. This causes that the α_i of the outer fibers to deviate from a desired linear change brought about by changes in γ_0, which greatly affects the shape sensing accuracy. Therefore, we propose a method to calibrate and compensate the fluctuation of inherent spin rate of MFS.

When MFS is continuously bent without twist in a single plane, θ_b can be calculated according to Eq. (2). Since there is no twist and three-dimensional distortion, θ_b reflects the rotational position of an outer fiber. That is the change of the inherent spin angle θ_0 of MFS. And γ_0 is the derivative of the θ_0 as

$$\gamma_0 = diff(\theta_0). \tag{15}$$

Since θ_0 is the inherent parameter of MFS, once calibrate the θ_0 along the fiber, its effects can be compensated by calculating θ_b in each cross-section according to Eq. (16).

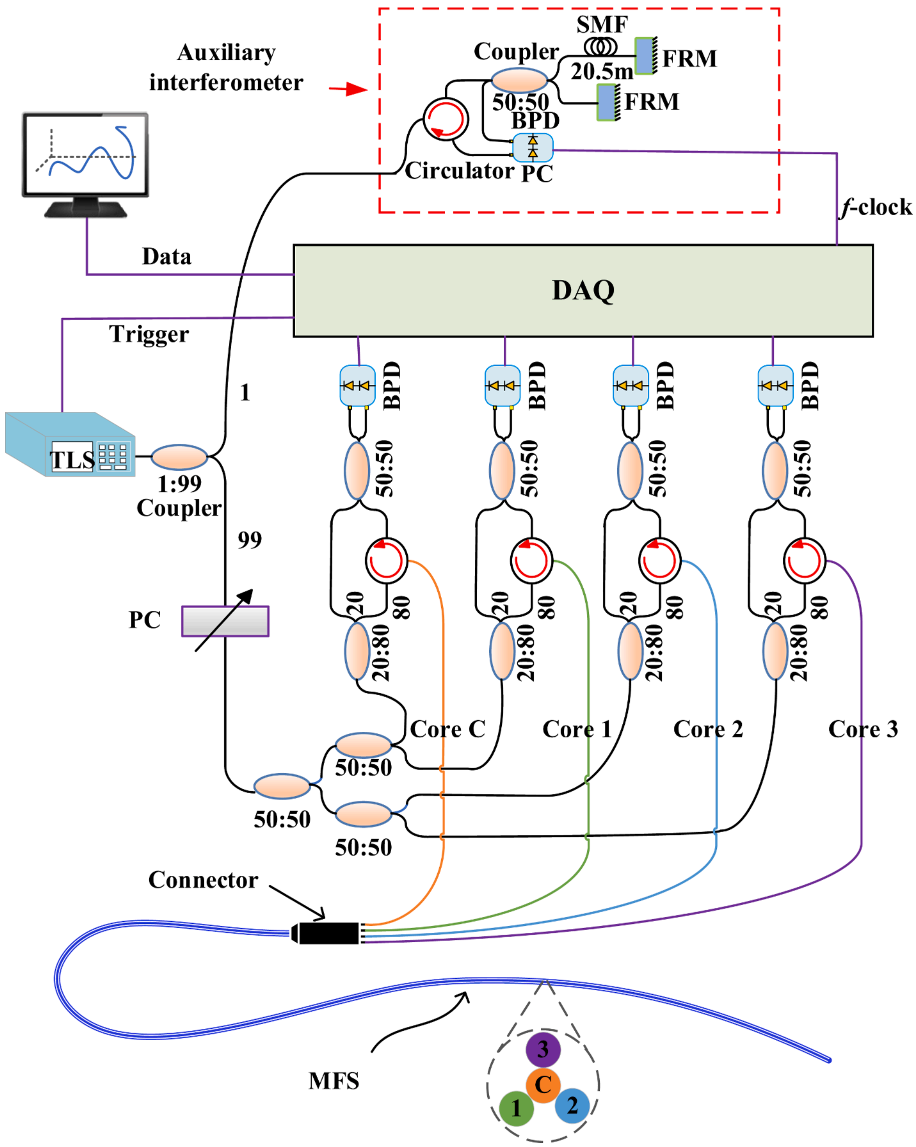

Fig. 9. Experiment setup of OFDR-based four-channels shape sensing system.

$$\theta_b = \arctan\left(\frac{\sum_{i=1}^{3}\frac{\varepsilon_i}{r}\sin(\alpha_i - \theta_0)}{\sum_{i=1}^{3}\frac{\varepsilon_i}{r}\cos(\alpha_i - \theta_0)}\right). \tag{16}$$

3. Experimental results and discussion

3.1. Experimental setup for shape sensing

Distributed 3D shape sensing system based on OFDR is shown in Fig. 9. The system is mainly composed of tunable laser (TLS, TLB-8800H, Newport Inc.), four-channels high-speed data acquisition card (DAQ, CSE1442, GaGe Inc.), auxiliary interferometer, four-channels main interferometer and MFS (3D_MF_G3A6-1.25, TSSC Inc.). The MFS consists of four continuous grating fibers that are tightly wound in a spiral, including three peripheral fibers at 120° to each other and a central fiber. MFS has a core spacing of 150 μm, a coating diameter of 455 μm and an inherent spin rate of 628 rad/m. The grating length of each core fiber is 10 mm. The grating spacing is 0.5 mm. The grating center wavelength is 1546 nm. The length of MFS is 1.2 m. MFS with continuous gratings can enhance signal to noise ratio (SNR) of Rayleigh scattering and improve the accuracy of shape sensing [16].

In the experimental setup, the test ends of the four-channels main interferometer are connected with the four core fibers of MFS, respectively. The light emitted from TLS is divided into two paths by a 1:99 fiber coupler. 1 % of the light enters the auxiliary interferometer, and passes through the circulator and 50:50 coupler to enter the reference arm and measuring arm of the auxiliary interferometer, respectively. A beat signal is generated at 50:50 coupler after reflection by two Faraday rotating mirrors (FRM). The beat signal is converted into an electrical signal by the Balanced Photodetector (BPD, PDB450C, Thorlabs Inc.) to provide an external clock for DAQ. The function of the clock trigger signal (*f*-clock) is to sample the beat signal of the main interferometer output at an equal optical frequency interval to compensate for the nonlinear tuning of TLS. 99 % of the light is divided into four channels after passes through a polarization controller (PC) and three 50:50 couplers, corresponding to the four core fibers of MFS. Each main interferometer is composed of 20:80 coupler, 50:50 coupler, reference arm and measuring arm. The optical signal of the measuring arm passes through the circulator and enters the core fiber of MFS. A beat interference occurs between Rayleigh backscattering returned in the core fiber of MFS and the reference light occurs in the 50:50 coupler. DAQ connect BPDs in these four channels of the main interferometer for analog-to-digital converting.

In the experiment, the tuning rate of TLS is $\gamma = 1500$ nm/s and the turning range is 18 nm from 1540 to 1558 nm, which corresponds to a total tuning time of 12 ms. The length of delay fiber of the auxiliary interferometer is 20.5 m so that the sampling rate and the spatial resolution of single data point are 37.5 M/s and 45 μm, respectively. The total length of the optical fiber under test is 5.8 m, and the length of the MFS under test is 1.1 m.

3.2. Calibration of inherent spin rate and coefficient between strain and differential phase

First, we need to conduct a set of calibration experiments to calibration initial spin rate of MFS and coefficient between strain and differential phase *K*. we collect a set of linear state data as a reference group, and make sure that MFS is in a natural state and there is no strain in MFS as far as possible. Then we place MFS in a single plane with a known radius and bend it continuously as a calibration group. The bending of MFS results in a periodic strain in the outer core fiber. The principle of strain demodulation in MFS is as described in Section 2.2. We demonstrate the process of differential phase strain demodulation in OFDR by taking one of outer fibers in

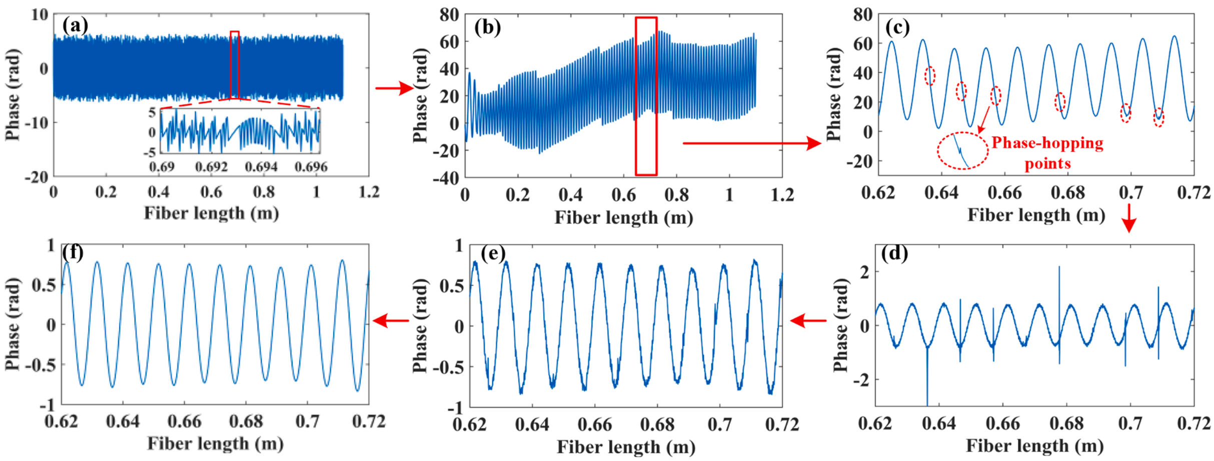

Fig. 10. Strain demodulation process. (a) Relative phase diagram. (b) Unwrapped relative phase diagram. (c) Local phase unwrapping diagram at the position of 0.62 m to 0.72 m. (d) Differential phase with outliers at the position of 0.62 m to 0.72 m. (e) Outliers removed differential phase using phase de-hopping filter. (f) Difference phase result after denoising at the position of 0.62 m to 0.72 m.

MFS as an example. Fig. 10 (a) shows the relative phase between the reference group and the calibration group. We find that the relative phase curve appears periodic due to the presence of the inherent spin of MFS. Phase unwrapping is performed on the data in Fig. 10 (a) to obtain the cumulative phase, as shown in Fig. 10 (b). In order to show the signal change process more clearly, we only show the results at the position of 0.62 m to 0.72 m in the subsequent processing. Fig. 10 (c) shows the local phase unwrapping diagram at the position of 0.62 m to 0.72 m. We can see from Fig. 10 (c) that there are some phase-hopping points due to TLS noise, which we can see more clearly by differentiating Fig. 10 (c) to get differential *2.2* to filter the outliers, the result is shown in Fig. 10 (e). It can be seen that Fig. 10 (e) still contains a lot of high-frequency noise that needs to be filtered. The experimental results after a phase low-pass filter for filtering are shown in Fig. 10 (f). The strain demodulation process of the measurement group is the same as that of the reference group and is not shown here.

Since MFS is continuously bent in a single plane, the theoretical θ_b should be a constant without the inherent spin of MFS. However, due to the existence of the inherent spin of MFS, θ_b will change constantly. Therefore, θ_b calculated by Eq. (2) is the inherent spin angle θ_0 of MFS when MFS is continuously bent on a single plane. And the γ_0 along MFS can be obtained by Eq.(15), as shown in Fig. 11. We find that γ_0 of MFS gradually increases from the starting point with a nominal value of 628 rad/m and γ_0 fluctuates slightly around the nominal value.

By bending MFS into a circle with a known radius, we can also calibrate the proportional coefficient between strain and differential phase K. The calibration method is to carry out the shape reconstruction experiment on the calibration group, and make the radius of the reconstructed circle consistent with the standard radius by constantly adjusting K. In the calibration group, the MFS is wound on a standard circular mold with a radius of 0.096 m, as shown in Fig. 12 (a). The shape reconstruction results are shown in Fig. 12 (b) and (c), and the final calibration $K = 2515$ με/rad.

3.3. External twist compensation and shape reconstruction

In this section, we will perform 3D shape reconstruction experiments to verify the proposed external twist and inherent spin rate compensation methods. After calibrating θ_0 and K, we can bend MFS into a complex 3D shape and collect data as a measurement group. We use circle segment algorithm to reconstruct the shape. According to the spatial resolution of the system, the length of each micro-segment is 45 μm, and the entire MFS with a 1.1 m length is divided into 24,444 segments. The experiment is carried out on a standard optical platform, which is convenient to determine the position coordinates of each point and calculate the shape reconstruction errors. In experiments, we use 3D printing technology to manufacture a cylindrical mold with standard spiral grooves. As shown in Fig. 13 (a), the diameter of the mold is 0.1 m and the height of the mold is 0.125 m. The mold is placed upside down on the X axis and 0.24 m away from the Y axis. We place MFS into the groove on the mold shown in Fig. 13 (a) and ensure that the end of MFS is at the highest point of the cylindrical mold. In this way, the position coordinates of the end of MFS can be determined as (0.240 m, 0.125 m, 0.100 m). The specific shape reconstruction steps and experimental results are as follows:

1) Use the differential phase strain demodulation algorithm in Section 2.2 to calculate the strain in each core fiber according to the data of the measurement group and the reference group.
2) Calculate the initial curvature κ along MFS according to Eq. (1). And use Eq. (16) to calculate θ_b after the inherent spin compensation according to the calibration results of θ_0.
3) Use Eq. (9), (12) and (13) to calculate γ_t of MFS, and Eq. (14) is used to compensate the external twist of MFS to acquire the compensated θ_b.
4) According to κ and θ_b, the shape reconstruction algorithm based on the circle segment [10] is used to reconstruct the shape.

The shape reconstruction results are shown in Fig. 13. Fig. 13 (b) is the three-dimensional curve of the shape reconstruction result, where the dashed line represents the standard curve, which is obtained by fitting multiple actual coordinate points. Fig. 13 (c), (d) and

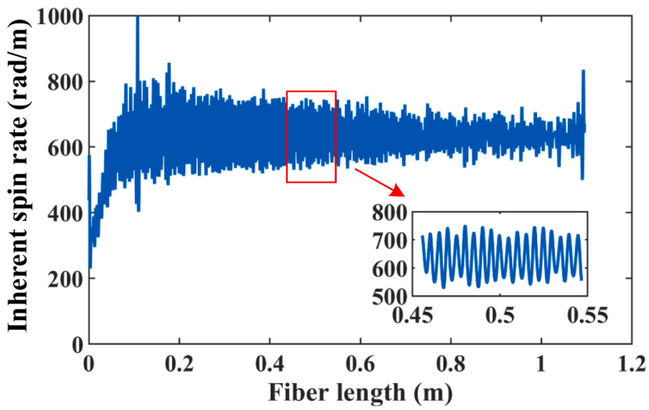

Fig. 11. Inherent spin rate varies along MFS.

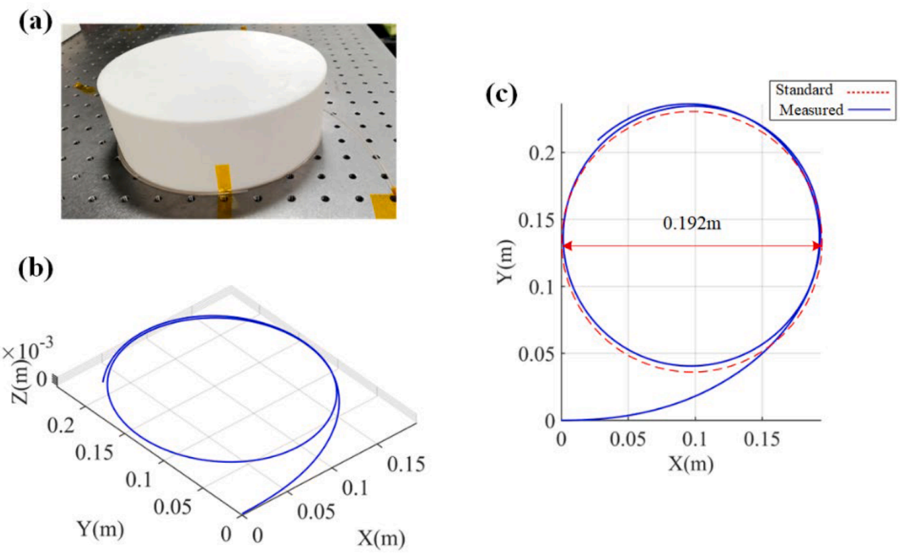

Fig. 12. Scale coefficient calibration experiment between differential phase and strain. (a) Actual diagram of fiber wound on a standard circular mold with a radius of 0.096 m. (b) Reconstructed curve of a circle in 3D graph. (c) A top view of the reconstructed curve of a circle with a diameter of 0.192 m.

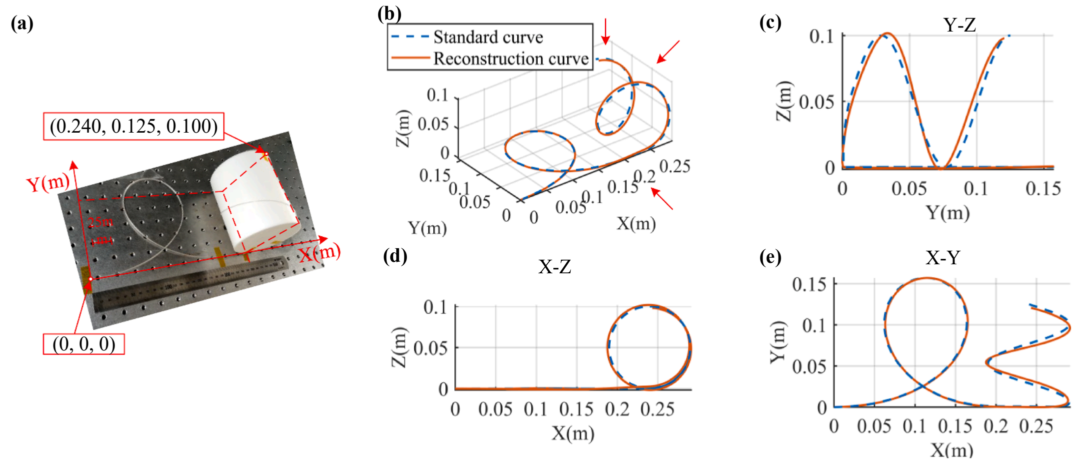

Fig. 13. Complex 3D shape reconstruction result. (a) Actual diagram of 3D curve reconstruction experiment, the distance between the two holes of the optical platform is 25 mm. (b) Reconstruct the 3D graph. (c) 2D view of curves in Y-O-Z plane. (d) 2D view of curves in X-O-Z plane. (e) 2D view of curves in X-O-Y plane.

(e) show the Y-Z, X-Z, and X-Y view respectively. We find that the reconstructed curve has a high consistency with the standard curve, which indicates that the proposed shape reconstruction method has a high sensing accuracy.

In order to quantitatively calculate the reconstruction error of the curve, we calculate the reconstruction error between the reconstructed curve and the standard curve every 5 mm along MFS. The reconstruction error is usually expressed by Euclidean distance error, which can be expressed as:

$$E_i = \sqrt{(x_i - x_i^0)^2 + (y_i - y_i^0)^2 + (z_i - z_i^0)^2}, \tag{17}$$

where (x_i, y_i, z_i) and (x_i^0, y_i^0, z_i^0) represent the coordinates of the reconstructed curve and the standard curve at a certain position, respectively. The Euclidean distance error curve along MFS is shown in Fig. 14. We take the maximum value on the curve as the maximum reconstruction error of the experiment. We find that the maximum reconstruction error occurs near the end of MFS, and the maximum reconstruction error is 6.7 mm, corresponding to a relative reconstruction error is 0.61 %.

In order to demonstrate the necessity of external twist and inherent spin rate compensation, 3D shape reconstruction experiments are carried out without external twist and inherent spin compensation, respectively. The experimental results are shown in Fig. 15 and

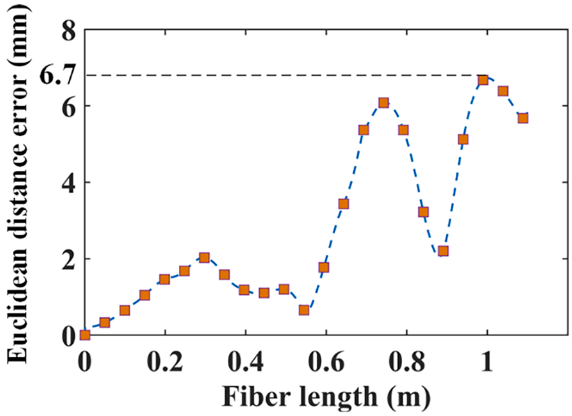

Fig. 14. Euclidean distance error curve along MFS when the shape in Fig. 12 is reconstructed.

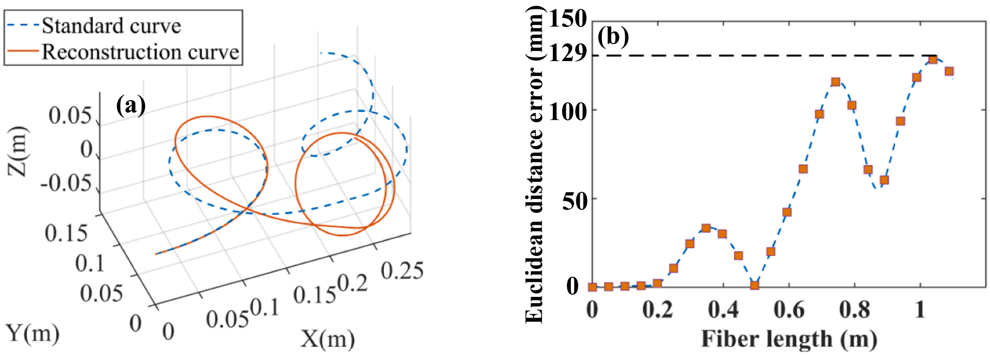

Fig. 15. Shape reconstruction results without external twist calibration. (a) Reconstructed curve without external twist compensation. (b) Euclidean distance error along MFS without external twist compensation.

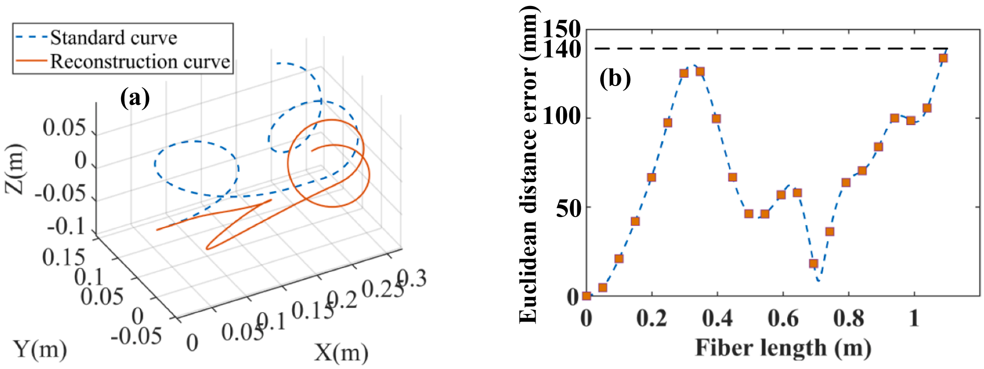

Fig. 16. Shape reconstruction results without inherent spin calibration. (a) Reconstructed curve without inherent spin compensation. (b) Euclidean distance error along MFS without inherent spin compensation.

Fig. 16. Fig. 15 shows the shape reconstruction results of MFS without external twist compensation. A comparison between the reconstructed three-dimensional curve and the standard curve is shown in Fig. 15 (a). Fig. 15 (b) is the Euclidean distance error curve along MFS. Similarly, we take the maximum Euclidean distance error along MFS as the reconstruction error of this experiment. It can be seen that the reconstruction error without external twist compensation is very large, the maximum reconstruction error is 129 mm, and the corresponding relative error reaches 11.7 %. The reconstruction accuracy after external twist compensation is 0.61 %, which increases more than 18 times compared with that before external twist compensation.

Fig. 16 shows the experimental results without inherent spin rate calibration. A comparison between the reconstructed three-dimensional curve and the standard curve is shown in Fig. 16 (a). Fig. 16 (b) is the Euclidean distance error curve along MFS. We find that the reconstruction error is also very large without inherent spin compensation, the maximum reconstruction error is 140 mm, corresponding to the relative error is 12.7 %. The reconstruction accuracy after inherent spin compensation is 0.61 %, which increases more than 20 times compared with that before inherent spin compensation. These two sets of experiments above show that external twist and the fluctuation of the inherent spin rate of MFS have a great influence on the shape reconstruction results, which must be compensated by the proposed method.

3.4. Comparison between shape sensing algorithm based on phase demodulation and cross-correlation demodulation

In order to prove that the proposed shape sensing algorithm based on phase strain demodulation has the advantages of high speed and high precision, we compare the proposed method with the traditional shape sensing algorithm based on cross-correlation strain demodulation in terms of demodulation accuracy and demodulation speed. In the comparison experiment of shape reconstruction accuracy, we use the same data to reconstruct a shape using these two algorithms, respectively. We compare the reconstructed curve with the standard curve and calculate their Euclidean distance errors along MFS. The experimental results are shown in Fig. 17. We find that these two shape reconstruction algorithms based on differential phase and cross-correlation have a similar shape reconstruction accuracy, and their maximum reconstruction errors are 6.7 mm and 6.2 mm, respectively, corresponding to the relative errors are 0.61 % and 0.56 %. The difference is so small that it is almost negligible in practice. In this experiment, we carry out a shape reconstruction with continuous frames. The time consumption on 1, 5, 10, 15 and 20 frames of shape reconstructions by the two methods are counted and the bar char is drawn in Fig. 18. We calculate the average completion time of 20 times shape reconstruction by these two methods. We find that the average time spent of the shape reconstruction method based on differential phase is only 104 ms, corresponding to the frame rate of about 10 Hz. In contrast, the average time of the cross-correlation based shape reconstruction method to complete a shape reconstruction is 940 ms, and its frame rate is only 1 Hz. Therefore, when the hardware is exactly the same, the speed of the proposed shape reconstruction algorithm is nearly 10 times higher than that of the traditional shape reconstruction algorithm based on cross-correlation. In fact, the frame rate of the proposed shape reconstruction algorithm in this paper can be further improved if FPGA or DSP is used for programming in the future. This is of great significance to the practical application of shape sensor.

4. Conclusion

In conclusion, we present a twist compensated, high accuracy and dynamic fiber optic shape sensing based on phase demodulation in OFDR. Firstly, a phase de-hopping filtering differential phase strain demodulation method is proposed and applied to shape sensing, which greatly improves the demodulation rate of shape sensing, and the spatial resolution reaches 45 μm. In addition, in order to eliminate the influence of external twist and fluctuation of inherent spin on the shape reconstruction results, we proposed an external twist compensation method and inherent spin rate calibration method, which greatly improved the shape measurement accuracy. The experimental results show that the reconstruction accuracies by the proposed external twist compensation and inherent spin rate calibration methods increase over 18 times and 20 times than those without these two methods respectively. By comparing with the traditional cross-correlation-based method, we find that the proposed shape sensing method based on phase demodulation has a similar reconstruction accuracy, the maximum reconstruction error is 0.61 %, whereas the shape reconstruction speed is improved by nearly 10 times.

CRediT authorship contribution statement

Sheng Li: Writing – original draft, Methodology, Data curation. **Qingrui Li:** Writing – original draft, Methodology, Data curation. **Zhenyang Ding:** Writing – review & editing, Supervision, Methodology, Conceptualization. **Kun Liu:** Supervision, Methodology,

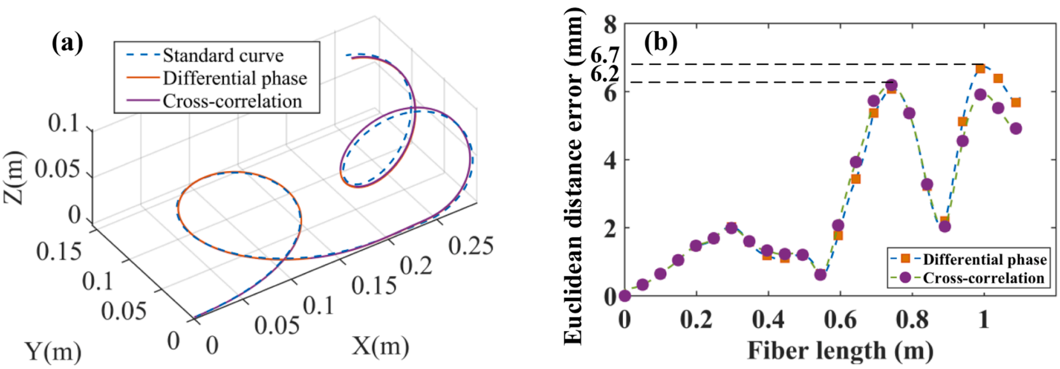

Fig. 17. Comparison of reconstruction accuracy of two shape reconstruction algorithms based on differential phase and cross-correlation. (a) Standard curve and shape reconstruction curves based on differential phase and cross-correlation method. (b) Euclidean distance error along fiber based on differential phase and cross-correlation method.

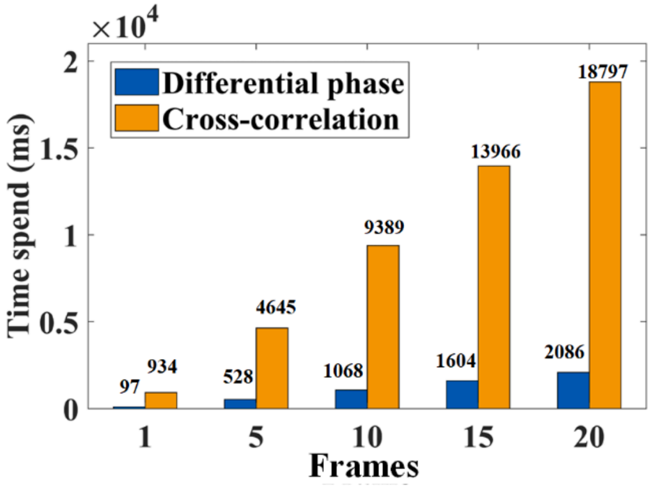

Fig. 18. Comparison of the time consumption by these two shape reconstruction algorithms based on differential phase and cross-correlation.

Conceptualization. **Huafang Wang:** Validation, Software, Data curation. **Peidong Hua:** Validation, Software, Data curation. **Haohan Guo:** Visualization, Resources, Investigation. **Teng Zhang:** Validation, Software, Data curation. **Ji Liu:** Validation, Software, Data curation. **Junfeng Jiang:** Supervision, Methodology, Conceptualization. **Tiegen Liu:** Writing – review & editing, Supervision, Methodology.

Declaration of competing interest

The authors declare that they have no known competing financial interests or personal relationships that could have appeared to influence the work reported in this paper.

Data availability

Data will be made available on request.

Acknowledgements

This work is supported in part by National Key Research and Development Program of China (2023YFF0715700), in part by National Natural Science Foundation of China (61975147).

References

[1] I. Floris, J.M. Adam, P.A. Calderón, S. Sales, Fiber optic shape sensors: A comprehensive review, Opt. Lasers Eng. (2021), https://doi.org/10.1016/j.optlaseng.2020.106508.
[2] J.P. He, Z. Zhou, J.P. Ou, Optic fiber sensor-based smart bridge cable with functionality of self-sensing, Mech Syst Signal Pr. 35 (2013) 84–94, https://doi.org/10.1016/j.ymssp.2012.08.022.
[3] H. Alian, S. Konforty, U. Ben-Simon, R. Klein, M. Tur, J. Bortman, Bearing fault detection and fault size estimation using fiber-optic sensors, Mech. Syst. Signal Process. 120 (2019) 392–407, https://doi.org/10.1016/j.ymssp.2018.10.035.
[4] A. Sultangazin, J. Kusmangaliyev, A. Aitkulov, D. Akilbekova, M. Olivero, D. Tosi, Design of a smartphone plastic optical fiber chemical sensor for hydrogen sulfide detection, IEEE Sens. J. 17 (2017) 6935–6940, https://doi.org/10.1109/Jsen.2017.2752717.
[5] A. Beisenova, A. Issatayeva, D. Tosi, C. Molardi, Fiber-optic distributed strain sensing needle for real-time guidance in epidural anesthesia, IEEE Sens. J. 18 (2018) 8034–8044, https://doi.org/10.1109/Jsen.2018.2865220.
[6] H. Moon, J. Jeong, S. Kang, K. Kim, Y.-W. Song, J. Kim, Fiber-Bragg-grating-based ultrathin shape sensors displaying single-channel sweeping for minimally invasive surgery, Optics Lasers Eng.. 59 (2014) 50–55, https://doi.org/10.1016/j.optlaseng.2014.03.005.
[7] F. Khan, R.J. Roesthuis, S. Misra, Force sensing in continuum manipulators using fiber Bragg grating sensors, Rep. U S. (2017) 2531–2536, https://doi.org/10.1109/IROS.2017.8206073.
[8] M.J. Gander, W.N. MacPherson, R. McBride, J.D.C. Jones, L. Zhang, I. Bennion, P.M. Blanchard, J.G. Burnett, A.H. Greenaway, Bend measurement using Bragg gratings in multicore fibre, Electron. Lett. 36 (2000) 120–121, https://doi.org/10.1049/el:20000157.
[9] L.W. Zhang, J.W. Qian, L.Y. Shen, Y.N. Zhang, FBG sensor devices for spatial shape detection of intelligent colonoscope, Front. Robot. A I (2004) 835–840, https://doi.org/10.1109/ROBOT.2004.1307253.
[10] R.J. Roesthuis, M. Kemp, J.J. van den Dobbelsteen, S. Misra, Three-dimensional needle shape reconstruction using an array of fiber Bragg grating sensors, IEEE/ASME Trans. Mechatron. 19 (2014) 1115–1126, https://doi.org/10.1109/tmech.2013.2269836.
[11] F. Khan, A. Denasi, D. Barrera, J. Madrigal, S. Sales, S. Misra, Multi-core optical fibers with bragg gratings as shape sensor for flexible medical instruments, IEEE Sens. J. 19 (2019) 5878–5884, https://doi.org/10.1109/jsen.2019.2905010.
[12] S. Jackle, T. Eixmann, H. Schulz-Hildebrandt, G. Huttmann, T. Patz, Fiber optical shape sensing of flexible instruments for endovascular navigation, Int. J. Comput. Assist. Radiol. Surg. 14 (2019) 2137–2145, https://doi.org/10.1007/s11548-019-02059-0.

[13] V. Modes, T. Ortmaier, J. Burgner-Kahrs, Shape sensing based on longitudinal strain measurements considering elongation, bending, and twisting, IEEE Sens. J. 21 (2021) 6712–6723, https://doi.org/10.1109/jsen.2020.3043999.
[14] K.J. Peters, R.G. Duncan, M.E. Froggatt, S.T. Kreger, R.J. Seeley, D.K. Gifford, A.K. Sang, M.S. Wolfe, High-accuracy fiber-optic shape sensing, Sensor Systems and Networks, Phenomena, Technology, and Applications for NDE and Health Monitoring (2007, 2007.), https://doi.org/10.1117/12.720914.
[15] P.S. Westbrook, T. Kremp, K.S. Feder, W. Ko, E.M. Monberg, H. Wu, D.A. Simoff, T.F. Taunay, R.M. Ortiz, Continuous multicore optical fiber grating arrays for distributed sensing applications, J. Lightwave Technol. 35 (2017) 1248–1252, https://doi.org/10.1109/jlt.2017.2661680.
[16] F. Parent, S. Loranger, K.K. Mandal, V.L. Iezzi, J. Lapointe, J.S. Boisvert, M.D. Baiad, S. Kadoury, R. Kashyap, Enhancement of accuracy in shape sensing of surgical needles using optical frequency domain reflectometry in optical fibers, Biomed, Opt. Express. 8 (2017) 2210–2221, https://doi.org/10.1364/BOE.8.002210.
[17] G. Yin, L. Lu, L. Zhou, C. Shao, Q. Fu, J. Zhang, T. Zhu, Distributed directional torsion sensing based on an optical frequency domain reflectometer and a helical multicore fiber, Opt. Express. 28 (2020) 16140–16150, https://doi.org/10.1364/OE.390549.
[18] S.T. Kreger, J.W. Klein, N.A.A. Rahim, J.J. Bos, Distributed Rayleigh scatter dynamic strain sensing above the scan rate with optical frequency domain reflectometry, in: Conference on Fiber Optic Sensors and Applications XII, 2015, https://doi.org/10.1117/12.2177578.
[19] C.H. Wang, K. Liu, Z.Y. Ding, J.F. Jiang, Z.E. Chen, Y.F. Feng, Y.Y. Zheng, Q.Q. Liu, T.G. Liu, High sensitivity distributed static strain sensing based on differential relative phase in optical frequency domain reflectometry, J. Lightwave Technol. 38 (2020) 5825–5836, https://doi.org/10.1109/Jlt.2020.3003584.
[20] S.Y. Zhao, J.W. Cui, Z.J. Wu, Z.Y. Wang, J.B. Tan, Distributed fiber deformation measurement by high-accuracy phase detection in OFDR scheme, J. Lightwave Technol. 39 (2021) 4101–4108, https://doi.org/10.1109/Jlt.2021.3055576.
[21] C. Fu, Y. Meng, L. Chen, H. Zhong, C. Du, J. He, X. Weng, L. Liu, J. Qu, Y. Wang, High-spatial-resolution φ-OFDR shape sensor based on multicore optical fiber with femtosecond-laser-induced permanent scatter arrays, Opt. Lett. 48 (2023) 3222, https://doi.org/10.1364/OL.486644.
[22] J.P. Moore, M.D. Rogge, Shape sensing using multi-core fiber optic cable and parametric curve solutions, Opt. Express. 20 (2012) 2967–2973, https://doi.org/10.1364/Oe.20.002967.
[23] K.C. Galloway, Y. Chen, E. Templeton, B. Rife, I.S. Godage, E.J. Barth, Fiber optic shape sensing for soft robotics, Soft Robot. 6 (2019) 671–684, https://doi.org/10.1089/soro.2018.0131.
[24] J. Villatoro, A. Van Newkirk, E. Antonio-Lopez, J. Zubia, A. Schulzgen, R. Amezcua-Correa, Ultrasensitive vector bending sensor based on multicore optical fiber, Opt. Lett. 41 (2016) 832–835, https://doi.org/10.1364/Ol.41.000832.
[25] H.-L. Liu, Z.-W. Zhu, Y. Zheng, B. Liu, F. Xiao, Experimental study on an FBG strain sensor, Optical Fiber Technol. 40 (2018) 144–151, https://doi.org/10.1016/j.yofte.2017.09.003.
[26] R. Xu, A. Yurkewich, R.V. Patel, Curvature, Torsion, and Force Sensing in Continuum Robots Using Helically Wrapped FBG Sensors, IEEE Robotics and Automation Letters. 1 (2016) 1052-1059.doi: 10.1109/lra.2016.2530867.
[27] C.G. Askins, G.A. Miller, E.J. Friebele, Bend and twist sensing in a multiple-core optical fiber, 2008 Conference on Optical Fiber Communication/National Fiber Optic Engineers Conference, Vols 1-8. (2008) 1545-1547.doi: 10.1109/OFC.2008.4528404.
[28] I. Gannot, P.S. Westbrook, K.S. Feder, T. Kremp, T.F. Taunay, E. Monberg, J. Kelliher, R. Ortiz, K. Bradley, K.S. Abedin, D. Au, G. Puc, Integrated optical fiber shape sensor modules based on twisted multicore fiber grating arrays, Optical Fibers and Sensors for Medical Diagnostics and Treatment Applications XIV (2014), https://doi.org/10.1117/12.2041775.
[29] I. Floris, J. Madrigal, S. Sales, P.A. Calderón, J.M. Adam, Twisting measurement and compensation of optical shape sensor based on spun multicore fiber, Mech. Syst. Signal Process. 140 (2020), https://doi.org/10.1016/j.ymssp.2020.106700.
[30] S. Lim, S. Han, Shape estimation of a bent and twisted cylinder using strain from a sensor array in triple helices, Meas. Sci. Technol. 29 (2018), https://doi.org/10.1088/1361-6501/aacfb6.
[31] I. Gannot, R. Xu, A. Yurkewich, R.V. Patel, Shape sensing for torsionally compliant concentric-tube robots, Optical Fibers and Sensors for Medical Diagnostics and Treatment Applications XVI (2016), https://doi.org/10.1117/12.2213128.
[32] https://shapesensing.com/trailblazer-development-platform (n.d.).
[33] C.D. Butter, G.B. Hocker, Fiber optics strain gauge, Appl. Opt. 17 (1978) 2867–2869, https://doi.org/10.1364/AO.17.002867.
[34] T. Pham-Gia, T.L. Hung, The mean and median absolute deviations, Math Comput Model. 34 (2001) 921–936, https://doi.org/10.1016/S0895-7177(01)00109-1.